

SMA OBSERVATIONS OF C₂H IN HIGH-MASS STAR FORMING REGIONS

XUE-JIAN JIANG(蒋雪健)^{1,2,3,4}, HAUYU BAOBAB LIU⁵, QIZHOU ZHANG², JUNZHI WANG⁶, ZHI-YU ZHANG^{7,8}, JUAN LI⁶, YU GAO¹ AND QIUSHENG GU^{3,4}

June 2015, *ApJ* accepted

ABSTRACT

C₂H is a representative hydrocarbon that is abundant and ubiquitous in the interstellar medium (ISM). To study its chemical properties, we present Submillimeter Array (SMA) observations of the C₂H $N=3-2$ and HC₃N $J=30-29$ transitions and the 1.1 mm continuum emission toward four OB cluster-forming regions, AFGL 490, ON 1, W33 Main, and G10.6-0.4, which cover a bolometric luminosity range of $\sim 10^3-10^6 L_{\odot}$. We found that on large scales, the C₂H emission traces the dense molecular envelope. However, for all observed sources, the peaks of C₂H emission are offset by several times 10^4 AU from the peaks of 1.1 mm continuum emission, where the most luminous stars are located. By comparing the distribution and profiles of C₂H hyperfine lines and the 1.1 mm continuum emission, we find that the C₂H column density (and abundance) around the 1.1 mm continuum peaks is lower than those in the ambient gas envelope. Chemical models suggest that C₂H might be transformed to other species owing to increased temperature and density; thus, its reduced abundance could be the signpost of the heated molecular gas in the $\sim 10^4$ AU vicinity around the embedded high-mass stars. Our results support such theoretical prediction for centrally embedded $\sim 10^3-10^6 L_{\odot}$ OB star-forming cores, while future higher-resolution observations are required to examine the C₂H transformation around the localized sites of high-mass star formation.

Keywords: astrochemistry; ISM: abundances; molecular processes; stars: early-type; stars: formation; stars: individual (G10.6-0.4, ON 1, W33 and AFGL 490)

1. INTRODUCTION

Observations have shown that high-mass stars form in massive molecular clumps on scales of 0.1–1 pc (e.g., Palau et al. 2007; Galván-Madrid et al. 2009; Zhang et al. 2009; Wang et al. 2012; Liu et al. 2011; Liu et al. 2012a,b; Galván-Madrid et al. 2013; Wang et al. 2014; Lu et al. 2014). The strong protostellar feedback in radiative pressure and mechanical processes (e.g. outflows, stellar wind) starts to disturb the ambient molecular gas while the massive stars are still deeply embedded (Zinnecker & Yorke 2007). How the contracting clumps dynamically evolve under the influence of the (proto)stellar feedback remains uncertain (e.g. Beuther et al. 2007; Krumholz et al. 2014). Extensive modelings have suggested that this feedback may leave chemical footprints (e.g. Lahuis & van Dishoeck 2000; Chapman et al. 2009; Herbst & van Dishoeck 2009; Tan et al. 2014). High spa-

tial resolution observations of molecular lines from fast-evolving (10^4-10^6 yr) clouds are therefore helpful to diagnose the history of cloud contraction and massive star formation even in the embedded phases.

Ethynyl radical (C₂H) is the simplest hydrocarbon molecule with the C \equiv C bond, which is closely related to the formation and transformation of long carbon chains and other hydrocarbons (Pilleri et al. 2013). C₂H and its predecessor C₂H₂ are crucial intermediates in the chemistry of aromatic rings (e.g., C₆H₆) and polycyclic aromatic hydrocarbon (PAH, Tielens 2013). However, because of its symmetry, C₂H₂ does not have a permanent dipole moment, so C₂H₂ lacks of rotational transitions, which makes C₂H₂ observationally challenging. On the other hand, C₂H has many strong emission lines accessible in millimeter bands. In addition, the hyperfine structure lines (HFS) of C₂H can provide estimates of optical depth and magnetic field by measuring the Zeeman effect. Its dipole moment (0.77 Debye, Wilson & Green 1977) is about seven times higher than that of CO, and it has a critical density of $\sim 10^5 \text{ cm}^{-3}$ (Sakai et al. 2010a).

C₂H was first detected in Galactic star-forming regions by Tucker et al. (1974), who derived a comparable C₂H abundance with those of HCN and HCO⁺. Later surveys found that C₂H is widespread over the inner Galactic plane (Liszt 1995), and it mainly arises from relatively dense gas (i.e. $n(\text{H}_2) \sim 10^4 - 10^5 \text{ cm}^{-3}$, Watt et al. 1988). C₂H has been detected in all evolutionary stages of high-mass star formation, e.g. infrared dark cloud (IRDC), prestellar cores, high-mass protostellar objects (HMPOs) and hot molecular cores (HMCs) (Wootten et al. 1980; Beuther et al. 2007; Li et al. 2012). Moreover, extragalactic studies show that C₂H is also quite strong, after those popular (dense)

Email: xjjiang@pmo.ac.cn

¹ Purple Mountain Observatory & Key Laboratory for Radio Astronomy, Chinese Academy of Sciences, 2 West Beijing Road, Nanjing 210008, P.R.China

² Harvard-Smithsonian Center for Astrophysics, 60 Garden St., Cambridge, MA 02138, USA

³ Key Laboratory of Modern Astronomy and Astrophysics, Nanjing University, Ministry of Education, Nanjing 210093, P.R.China

⁴ Collaborative Innovation Center of Modern Astronomy and Space Exploration, Nanjing 210093, China

⁵ Academia Sinica Institute of Astronomy and Astrophysics, P.O. Box 23-141, Taipei 106, Taiwan

⁶ Shanghai Astronomical Observatory, Chinese Academy of Sciences, 80 Nandan Road, Shanghai 200030, P.R.China

⁷ Institute for Astronomy, University of Edinburgh, Royal Observatory, Blackford Hill, Edinburgh EH9 3HJ, United Kingdom

⁸ ESO, Karl Schwarzschild Strasse 2, D-85748 Garching, Munich, Germany

gas tracers HCN, HNC, HCO^+ , CS, etc., so it can be used in multi-molecule diagnosis on galactic environment (e.g., Meier & Turner 2005, 2012; Meier et al. 2015; Jiang et al. 2011; Imanishi & Nakanishi 2014).

Single-dish and interferometric observations toward HMPo and ultracompact HII (UCHII) regions found that C_2H abundance is decreasing toward the central hot cores (Beuther et al. 2008; Pilleri et al. 2013), which suggests that C_2H can trace cold molecular gas in the early phase of star formation (see also Gerin et al. 2011). Observations on prestellar cores (Padovani et al. 2009) also found similar trends of C_2H abundance and implied that the sizes of C_2H depletion holes are a few thousand AU. Mookerjee et al. (2012) compared the distributions and abundances of C_2H and C_3 in DR 21 (OH) and suggested the chemical (gas-phase) timescale for these species to be $\sim 0.7 - 3$ Myr. The aforementioned results, however, are still limited by spatial resolution and biased samples. A systematic survey will help clarify the environmental effects and will help us understand the formation and evolution of C_2H in massive star-forming regions.

In this paper, we present the Submillimeter Array (SMA)¹ observations of the C_2H $N = 3 - 2$ transitions toward four massive star-forming regions, G10.6-0.4, W33 Main, ON 1, and AFGL 490. These samples were selected from the previous single-dish mapping survey of C_2H 1-0 (87.317 GHz), HNC 1-0 (90.664 GHz), and HC_3N 10-9 (90.979 GHz) in 27 high-mass star forming regions (Li et al. 2012), using the Purple Mountain Observatory 14m Telescope (PMO-14m; HPBW $\sim 55''$). The accurate parallax distances have been measured except for AFGL 490, whose distance has an uncertainty of $\sim 50\%$. Details of our observations and data reduction are given in Section 2. We present the observational results in Sections 3.1. The analysis of the C_2H optical depth and abundance profiles are provided in Section 3.2 and 3.3. The implications of our results are discussed in Section 4.

2. OBSERVATIONS AND DATA REDUCTION

The SMA observations were carried out on 2012 August 4, with six available antennae in the subcompact configuration. The phase referencing and pointing centers coincide with the water maser positions in the selected targets (see Li et al. 2012). The weather condition was moderate ($\tau_{225\text{ GHz}} \sim 0.25$), yielding a typical system temperature T_{sys} of ~ 300 K. The passband calibrator is 3C 279, and the flux calibrators are Titan/Callisto. The absolute fluxes are accurate to within 15%.

The observations covered a frequency range of about 259–263 GHz in the lower sideband and 271–275 GHz in the upper sideband. Our observations covered the C_2H $N=3 \rightarrow 2$, $J=7/2 \rightarrow 5/2$, $F=4 \rightarrow 3$, $\nu_{\text{rest}}=262.00426$ GHz (blended with the $F=3 \rightarrow 2$ line), and $J=5/2 \rightarrow 3/2$, $F=3 \rightarrow 2$, $\nu_{\text{rest}}=262.06499$ GHz (blended with the $F=4 \rightarrow 3$ line). These are the two main groups of the C_2H $N = 3 - 2$ hyperfine structures. We simultaneously obtained HC_3N $J = 30 - 29$ ($E_u \sim 203$ K), which is an excellent tracer of HMCs (Chapman et al. 2009;

Meier & Turner 2012). A uniform spectral channel spacing was set to be 0.8125 MHz ($\sim 0.93 \text{ km s}^{-1}$) across the entire passband. The SMA data were calibrated using the MIR IDL software package.² We use the line-free channels in both the lower and upper sidebands to generate the continuum channels, which are then imaged jointly to produce the 1.1 mm continuum image. The continuum emission is subtracted before performing the spectral line imaging. The imaging is carried out using the CASA (McMullin et al. 2007) package, with uniform weighting and hogbom CLEANing algorithm. We do not perform primary beam corrections since the angular sizes of the emission are small compared with the SMA primary beam ($\sim 1'$). In addition, the primary beam effects are factored out when we analyze the intensity ratios (see section 3.3). Table 1 lists the observational properties of these sources, including the integration time, and the bolometric luminosities of these sources.

3. RESULTS

3.1. The C_2H $N=3-2$ brightness distribution

Figure 1 shows the integrated intensity maps of C_2H $N=3-2$ ($E_u \sim 25$ K), which are overlaid with the 1.1 mm continuum emission (white contours) and HC_3N $J=30-29$ integrated intensity (cyan contours). The 1.1 mm continuum emission may be contaminated by both the dust thermal emission and the free-free emission from the UC HII regions. The high-excitation HC_3N $J=30-29$ line ($E_u \sim 203$ K) helps locate the HMCs. We resolved the extended C_2H emission surrounding the continuum peaks (Figure 1), while the previous single-dish observations of the lower excited C_2H $N=1-0$ line ($E_u \sim 4$ K) traced the diffuse emission from a more extended area (Li et al. 2012). The size and geometry of the warm molecular gas traced by C_2H $N = 3 - 2$ are consistent with those traced by other molecular lines (e.g. G10.6-0.4: Liu et al. 2010; W33 Main: Haschick & Ho 1983), suggesting that the resolved C_2H $N = 3 - 2$ brightness distributions are likely not strongly biased by missing flux (Section 4). The peaks of C_2H $N=3-2$ emission and continuum have systematic offsets. We do not resolve ring-like C_2H distribution found in Beuther et al. (2008) and Guélin et al. (1999), likely because of the projection (or inclination) of the sample and the insufficient angular resolution of the observations.

Figure 2 shows the intensity-weighted velocity maps. The C_2H 3–2 emission shows velocity gradients, while its centroid velocities are comparable with the systemic velocities. More information about the individual targets is provided as follows. The measurements of the rms noise of the maps and the fluxes of C_2H 3-2 are listed in Table 2. We achieve $\sim 6''$ angular resolution in the final images.

G10.6-0.4 — The UCHII region G10.6-0.4 (Ho & Haschick 1986; Keto et al. 1987, 1988; Sollins et al. 2005; Liu et al. 2010; Liu et al. 2010; Liu et al. 2011) is a well-studied OB cluster-forming region (Ho & Haschick 1981; Liu et al. 2013), which is deeply embedded in the convergence of several ~ 5 pc scale dense gas filaments. Adopting the parallax

¹ Submillimeter Array is a joint project between the Smithsonian Astrophysical Observatory and the Academia Sinica Institute of Astronomy and Astrophysics and is funded by the Smithsonian Institution and the Academia Sinica.

² The MIR Cookbook by Chunhua Qi can be found at <http://cfa-www.harvard.edu/~cqi/mircook.html>

Table 1
General observational properties of the sample

(1) Source	(2) R.A. (J2000) (h m s)	(3) Dec (° ' ")	(4) Distance (kpc)	(5) Luminosity (L_{\odot})	(6) Int.time (minutes)
G10.6-0.4	18:10:28.70	−19:55:48.7	4.95	7×10^5	120
W33 Main	18:14:13.67	−17:55:25.2	2.40	5.4×10^5	107
ON 1	20:10:09.14	31:31:37.4	2.35	2.7×10^4	120
AFGL 490	03:27:38.80	58:47:00.0	1.0	2×10^3	100

Note. — (1) Source names; (2) and (3) coordinates of the phase centers; (4) Distances of the sources. Parallax distances of G10.6-0.4 from Sanna et al. (2013), W33 from Immer et al. (2013), and ON1 from Xu et al. (2013); (5) Bolometric luminosities, converted from previous values using the latest parallax distances, if available; (6) On-source integration time.

Table 2
Measurements

(1) Source	(2) Beam (")	(3) RMS _{cont} (Jy beam ^{−1})	(4) RMS _{C₂H} (Jy beam ^{−1} km s ^{−1})	(5) RMS _{HC₃N} (Jy beam ^{−1} km s ^{−1})	(6) S_{C_2H} (Jy km s ^{−1})	(7) Δv^a (km s ^{−1})
G10.6-0.4	7.3×6.0	0.20	8.0	2.0	590	[−10.7, 2.8]
W33 Main	7.2×5.9	0.12	3.4	2.6	212	[27.0, 40.5]
ON 1	6.5×5.6	0.04	0.97	1.3	75.4	[7.4, 14.6]
AFGL 490	8.9×5.0	0.02	0.83	...	41.0	[−17.1, −11.7]

Note. — (1) Source names; (2) Synthesized beam (uniform-weighted) of the images; (3) 1 σ RMS of the continuum images; (4) 1 σ RMS of the C₂H $N=3-2$ moment zero maps; (5) 1 σ RMS of the HC₃N $J=30-29$ moment zero maps; (6) Integrated flux of C₂H $N=3-2$; (7) Velocity ranges of the C₂H 3-2 (7/2–5/2, 4–3) Main line. Note that the rms values listed here are higher than the expected thermal noise in the data since they are limited by the dynamic range in the images.

distance of 4.95 kpc (Sanna et al. 2013), its bolometric luminosity is about $7 \times 10^5 L_{\odot}$ (note that the luminosities for all the sources in this paper are recalculated with their parallax distances, if available).

On the ~ 0.5 pc scale, the C₂H $N = 3 - 2$ emission (Figure 2) shows an obvious velocity gradient, and it likely traces the edge-on spinning-up molecular accretion flow resolved by the previous observations of highly excited NH₃ lines (Ho & Haschick 1986; Keto et al. 1987; Liu et al. 2010). The channel maps of C₂H $N = 3 - 2$ (Figure 3) demonstrate the known southeast–northwest velocity gradient in this flattened accretion flow (Keto et al. 1987; Liu et al. 2010). The integrated intensity of C₂H peaks at both blueshifted and redshifted lobes, which locate to the SE and NW. It shows weaker emission at the center. We also notice that the C₂H emission is weaker in the west of the region, where the other two UC HII regions reside (red asterisks in Figure 1 and 2).

W33 Main— W33 Main (G12.8-0.2) resides in the OB cluster-forming region W33 Complex (Haschick & Ho 1983). At a distance of 2.4 kpc (Immer et al. 2013), its bolometric luminosity is about $5.4 \times 10^5 L_{\odot}$. In our observations, the 1.1 mm continuum (~ 3 Jy) peaks at R.A.(2000) = 18^h14^m13.8^s, decl.(2000) = −17°55′43.4″, which is associated with the infrared source IRS 3 (Dyck & Simon 1977) and the centimeter peak W33 Main-B2. The distribution of HC₃N 30–29, however, is slightly different and is closer to another centimeter emission peak, B1 (Haschick & Ho 1983). We also detect another 1.1 mm source associated with the IRS 2 and

the UC HII region W33 Main-A in the north. It shows weaker emission in 1.1 mm continuum (~ 0.6 Jy) and in the HC₃N 30–29 transition, comparing to the south component.

As shown in Figure 1, the C₂H $N = 3 - 2$ emission is mainly distributed around W33 Main-A and W33 Main-B. The emission of C₂H 3-2, HC₃N 30–29 and 1.1 mm continuum around W33 Main-B are brighter and appear to be offset from each other, while in W33 Main-A their peak positions agree better with each other. The environment of W33 Main is quite complicated since there are multiple (UC)HII regions, and these (UC)HII regions A, B1, and B2 seem to be embedded in the gas envelope traced by C₂H 3-2. Although the projection effect cannot be ruled out, the differences between these two regions (W33 Main-A and B) could be explained by their different physical conditions and star-forming activities. Comparing with W33 Main-A, W33 Main-B is much more massive and brighter in infrared, millimeter, and centimeter continuum, as well as consisting of more HII regions (Haschick & Ho 1983). As revealed by the continuum and HC₃N on ~ 0.1 pc scales in Figure 1, the different behaviors of B1 and B2 also suggest that these two regions have different stages of SF process. The velocity field in W33 Main-B is complicated (Figure 2), which suggests influence from the multiple molecular outflows (Immer et al. 2014).

ON 1— The UC HII region Onsala 1 (ON 1) is a cluster-forming region with multiple star-forming signposts (Kumar et al. 2003; Su et al. 2009). At a parallax distance of 2.35 kpc (Xu et al. 2013) its luminosity is about

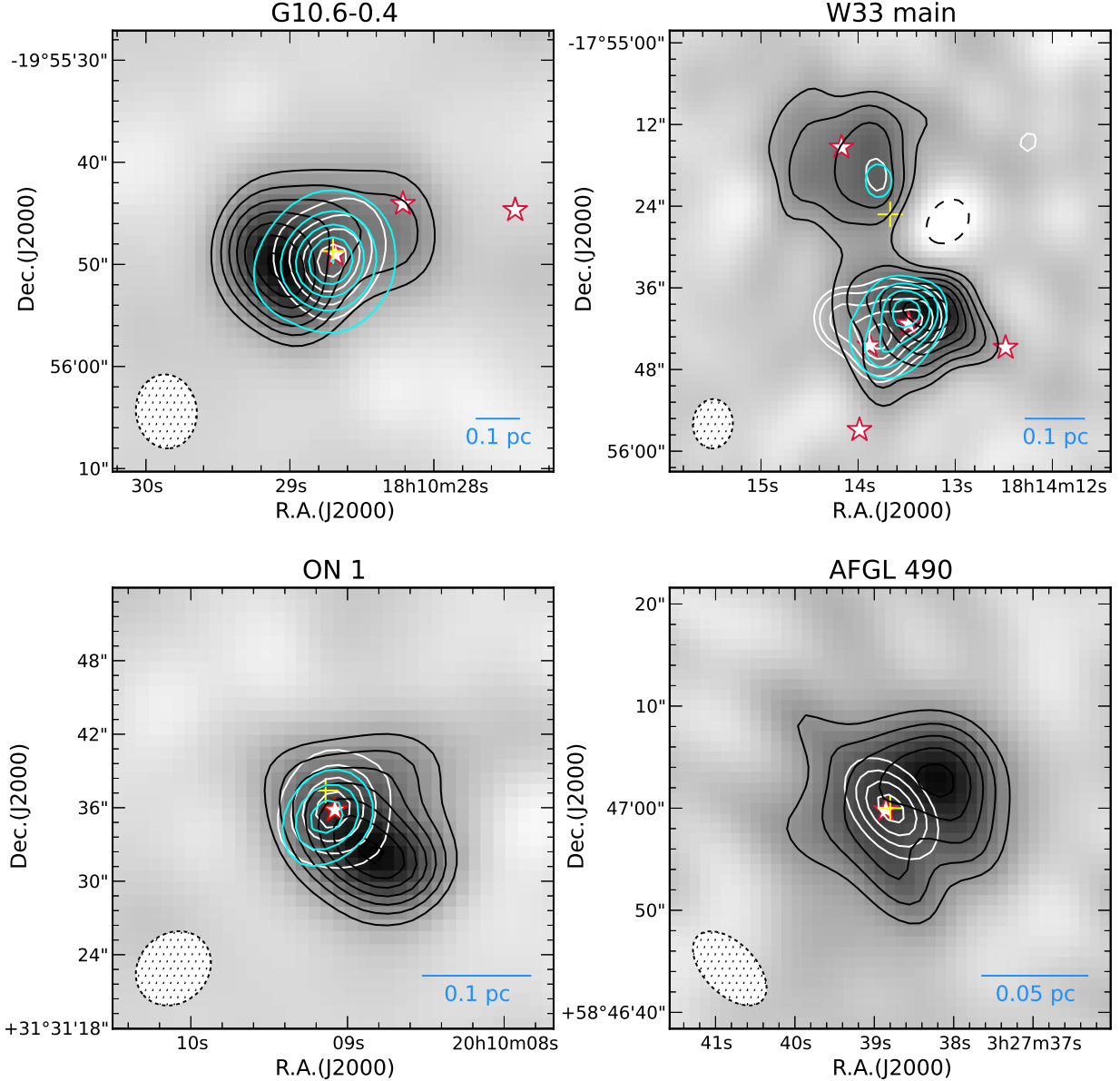


Figure 1. Grayscale and black contours are the $\text{C}_2\text{H } N = 3 - 2$ ($J = 7/2 - 5/2$, $F = 4 - 3$) uniformly weighted moment zero (integrated intensity) maps of G10.6-0.4, W33, ON 1 and AFGL 490, respectively. C_2H intensity levels (black contours) start from the 5σ level and continue in 3σ steps. The white contours are the 1.1 mm continuum images (30%, 50%, 70%, and 90% the peak emission). The continuum peaks are 8.0, 4.1, 1.8, and 2.0 Jy beam^{-1} , respectively. The cyan contours are $\text{HC}_3\text{N } J = 30 - 29$ uniformly weighted moment zero maps. In G10.6-0.4 the $\text{HC}_3\text{N } 30-29$ contours start from the 5σ level and continue in 10σ steps. In W33 Main and ON 1 the $\text{HC}_3\text{N } 30-29$ contours start from the 4σ level and continue in 3σ steps. The 1σ of the continuum, $\text{C}_2\text{H } 3-2$ and $\text{HC}_3\text{N } 30-29$ are listed in Table 2. The red asterisks denote the positions of the (UC) HII regions (Ho & Haschick 1986; Haschick & Ho 1983; Kumar et al. 2004; Simon et al. 1983). The yellow crosses denote the position of the H_2O masers. The SMA subcompact synthesis beams of the C_2H images are shown in the bottom left corners. *A colorful figure is available in the online version.*

$2.7 \times 10^4 L_\odot$ (MacLeod et al. 1998). Figure 1 shows that the 1.1 mm continuum and the $\text{HC}_3\text{N } J = 30 - 29$ emission both agree well with the center of the UC HII and the H_2O maser, while the $\text{C}_2\text{H } N=3-2$ emission peaks show offsets in the southwest. Figure 2 shows that C_2H has a velocity gradient along the northeast-southwest direction, and the velocity at the emission peak is consistent with the systemic velocity $v_{\text{LSR}} = 12 \text{ km s}^{-1}$ (Su et al. 2009). Such distribution along the NE-SW direction

is in agreement with the H^{13}CO^+ distribution reported by Kumar et al. (2004), which is interpreted as one of the multiple molecular outflows in ON 1, while high-resolution observations toward the innermost region by Su et al. (2009) favor a scenario of the expansion of the HII region. Other than the main SW component, Figures 1 and 2 also show that the C_2H emission appears to slightly extend to the northwest, in a direction perpendicular to the proposed bipolar outflow (or expansion

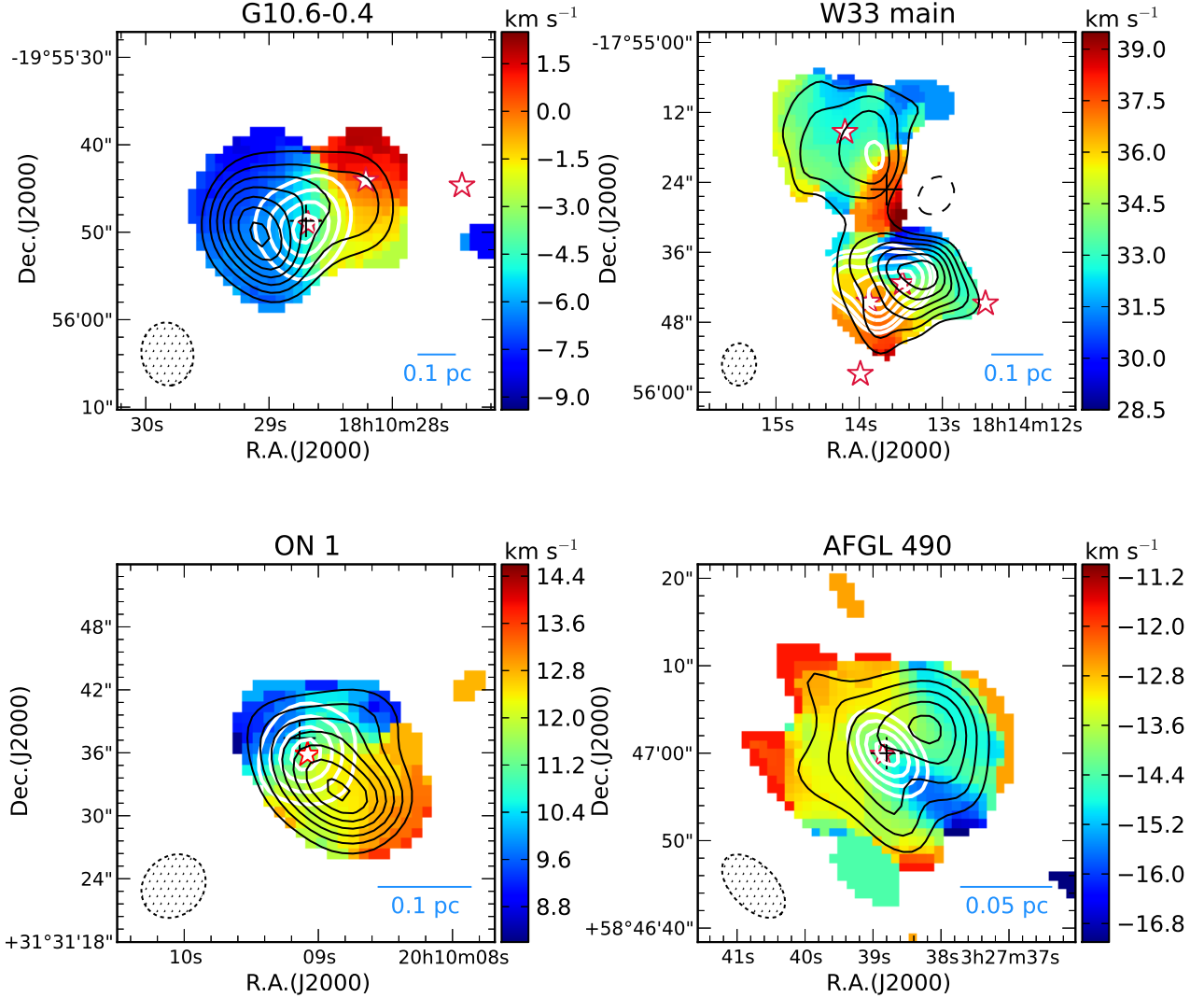


Figure 2. Moment one (intensity-weighted average velocity) maps of C₂H $N = 3 - 2$ ($J = 7/2 - 5/2$, $F = 4 - 3$) of G10.6-0.4, W33, ON 1 and AFGL 490. The black contours are the C₂H 3-2 moment zero, and the white contours are the 1.1 mm continuum, as shown in Figure 1. The asterisks and crosses denote the (UC)HII regions and the H₂O masers. The SMA subcompact synthesis beams ($\sim 6''$) are shown in the bottom left corners. *A colorful figure is available in the online version.*

motion). This component might be related to the other outflow component traced by SiO and CO as reported by Kumar et al. (2004). These authors derived that the central enclosed mass of ON 1 is about 300–400 M_{\odot} , which would be sufficient to support a rotating structure, so with current data we are not yet able to rule out the possibility of a flattened rotating accretion flow confining the UCHII region.

AFGL 490— AFGL 490 is a deeply embedded 8–10 M_{\odot} young star. Previous CO and ¹³CO observations suggest a warm ($T_{\text{kin}} \gtrsim 100$ K) gas component within the central ≈ 6000 AU radius, surrounded by a cooler gas

envelope (Mitchell et al. 1995). Schreyer et al. (2002) reported that the size of the outer envelope is about 22,000 AU \times 6000 AU. Molecular outflows have also been inferred from the detection of high-velocity CO emission (Mitchell et al. 1995).

In AFGL 490 C₂H 3-2 is significantly weaker than that in other sources, and HC₃N 30-29 is not detected. The brightness distribution of C₂H $N = 3 - 2$ mainly follows the flattened dense gas envelope traced by the CS $J = 3 - 2$ transition (Figure 1; Schreyer et al. 2002) and peaks at northwest of the 1.1 mm continuum source. The velocity gradient of C₂H $N=3-2$ in Figure 2 is not as

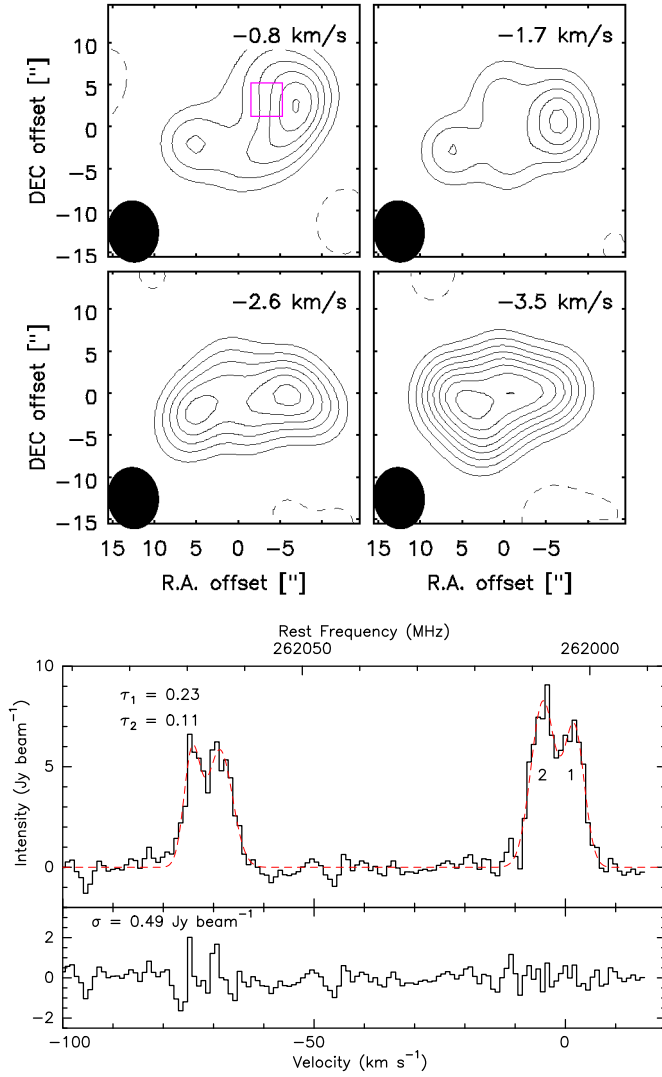


Figure 3. Examples of C₂H $N = 3 - 2$ channel maps of G10.6-0.4, from $V_{\text{LSR}} = -0.8 \text{ km s}^{-1}$ to -3.5 km s^{-1} . Contours start from 5σ and increase in 3σ steps (dashed contours are negative). The SMA subcompact synthesis beams are shown in the bottom left corners. A solid square in the first channel map denotes the position where we extract the spectrum in the bottom panel. The spectrum shows two velocity components of C₂H 3-2 emission in that position. Numbers “1” and “2” denote the main hyperfine groups of the two velocity components, and the red dashed line is the fitting to the spectrum. The fitting residual and corresponding RMS are shown below the spectrum. A colorful figure is available in the online version.

clear as in G10.6-0.4 or ON 1, but it still shows that the C₂H $N=3-2$ emission consistently traces the northwest-southeast velocity gradient in this flattened dense gas envelope, as well as the molecular gas wind perpendicular to the flattened envelope (Schreyer et al. 2002).

3.2. Optical depth of C₂H $N = 3 - 2$

The electron-nucleus interaction of C₂H results in six splitting hyperfine line components. Optical depth can be obtained by fitting the hyperfine structures. We extract the C₂H $N = 3 - 2$ spectra in every $\sim 3'' \times 3''$ pixels and fit the optical depth using the CLASS package,³ based

on the theoretical intensity ratios provided in the CDMS database⁴ (Müller et al. 2005). LTE relative line intensities were assumed. The bottom panel of Figure 3 shows an example spectrum of G10.6-0.4 extracted from a position offset from the core center (indicated by the solid square in the first channel map of Fig. 3). The spectrum shows two velocity components (line separation $\Delta V \sim 5 \text{ km s}^{-1}$, labeled ‘1’ and ‘2’), which would cause confusion in the fitting of hyperfine structures (the velocity separation of the two hyperfine lines of each group is about 2.54 km s^{-1}). We use Gaussian profiles to decompose the two velocity components, and then we derive their optical depths separately.

We found that C₂H is optically thin ($\tau \sim 0.1$) in most regions, which is comparable with the optical depth of C₂H found in the UCHII region MonR2 (Pilleri et al. 2013). Using a single-dish telescope Li et al. (2012) also found that the optical depths of C₂H are small to moderate in most massive star-forming regions. The estimates of the C₂H column density $N_{\text{C}_2\text{H}}$ and abundance $X_{\text{C}_2\text{H}}$ are given in section 3.3.

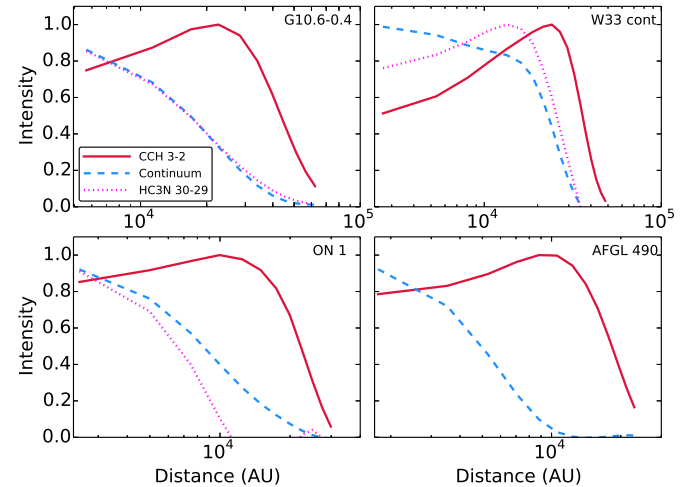


Figure 4. Normalized intensity profiles of different tracers (red solid lines: C₂H 3-2, blue dashed lines: continuum; magenta dotted lines: HC₃N 30-29) of the four sources, which are extracted and measured along a strip starting from the continuum peaks to the C₂H peaks. Horizontal axis is the distance from the continuum peaks. A colorful figure is available in the online version.

3.3. Intensity and column density profiles

The HC₃N $J = 30 - 29$ emission ($E_u \sim 203 \text{ K}$) provides a good probe of the dense and warm gas concentration. We did not detect HC₃N 30-29 in AFGL 490. For the rest of the sources, the normalized 1.1 mm continuum and the radial distributions of C₂H 3-2 and HC₃N 30-29 are presented in Figure 4. We use one strip from the continuum peak to the C₂H peak, to extract the intensity profile for each source, so as to show the relative offset scale of different tracers.

The C₂H 3-2 intensity increases outward until several times 10^4 AU separation from the 1.1 mm emission peak and then drops steeply. In G10.6-0.4 and ON 1,

³ <http://www.iram.fr/IRAMFR/GILDAS>

⁴ <http://www.astro.uni-koeln.de/cdms>

HC₃N 30-29 appears to be correlated with the 1.1 mm continuum emission and is confined in the compact regions (see also Figure 1). In W33 Main, HC₃N 30-29 peaks in between the peaks of the 1.1 mm continuum and the C₂H 3-2 emission, and HC₃N is very close to one of the H II region B1 (Figure 1). Nevertheless, the C₂H 3-2 emission peak is spatially offset from the 1.1 mm continuum and the HC₃N 30-29 emission peak in W33 Main.

To quantify the column density and abundance profiles of C₂H, we extract the C₂H 3-2 line intensity and the 1.1 mm continuum flux in several regions with diameter $\sim 3''$ from the continuum peak and through the C₂H 3-2 line emission peak, until the S/N drops to $< 2\sigma$ for either the 1.1 mm continuum or the C₂H 3-2 emission. Column densities of H₂ are derived from 1.1 mm continuum, following Beuther et al. (2002, 2005) and assuming an emissivity $\beta = 1.5$ and $\kappa_{1.2mm} = 0.97$. Following Hunter & Brogan (2006), the column density of C₂H, $N(\text{C}_2\text{H})$, is derived using

$$N(\text{C}_2\text{H}) = \frac{8\pi k\nu^2}{hc^3 A_{ul} g_u} \exp\left(\frac{E_u}{kT_{\text{ex}}}\right) \cdot S_{\text{C}_2\text{H}} \quad (1)$$

where A_{ul} , Q_t , g_u are the Einstein A coefficient, the partition function, and the upper-state degeneracy quoted from the CDMS, respectively. $S_{\text{C}_2\text{H}}$ is the line intensity of C₂H in units of K km s⁻¹. Identical $T_{\text{ex}} = 20$ K and $T_{\text{dust}} = 50$ K are adopted in the calculations for all the sources. Such an assumption on T_{dust} is consistent with previous values adopted for these sources (e.g., Liu et al. 2010; Haschick & Ho 1983; Kumar et al. 2004; Mueller et al. 2002; Schreyer et al. 2006), where the T_{ex} are found to be all close to 20 K in the hyperfine structure fittings of C₂H (Section 3.2), similar to the value derived by De Beck et al. (2012). We find that the derived $N(\text{C}_2\text{H})$ values are a few times 10¹⁵ cm⁻² for all targets.

There are several sources of errors in the estimates of the C₂H column density and abundance relative to the H₂ molecule. The variation of T_{ex} between 15 and 25 K can introduce up to 0.3 dex error in $\log N(\text{C}_2\text{H})$, so the typical error in $\log N(\text{C}_2\text{H})$ is about 0.4 dex considering the error on $S_{\text{C}_2\text{H}}$ of about 50%. The variation of T_{dust} between 40 and 60 K would also result in about 0.1 dex error in $\log N(\text{H}_2)$. Although adopting different values of β (e.g., $\beta = 1, 1.5, 2$) will introduce about 0.3 dex uncertainty in $\log N(\text{H}_2)$, we expect that β is probably similar in these sources. Uncertainties on the absolute fluxes of continuum and C₂H line are factored out as $X(\text{C}_2\text{H})$ is based on their intensity ratios. Thus, the typical error in $\log X(\text{C}_2\text{H})$ is about 0.5 dex. However, we caution that the derived C₂H column density and abundance profiles cannot be very precise at this moment. This is mainly because (1) part of the 1.1 mm continuum may be contaminated by free-free emission, which cannot be accurately subtracted yet, and (2) the missing fluxes in interferometric observations can lead to uneven underestimates of the continuum and line intensities. Thus, the results could be possibly affected by another factor of two. Nevertheless, as we used the SMA subcompact configuration with about 6'' resolution, those extended emissions on a scale of less than 1' (~ 1 pc; Li et al. 2012) should be recovered effectively, so we suppose that the amount of diffuse emissions should be limited and the results are

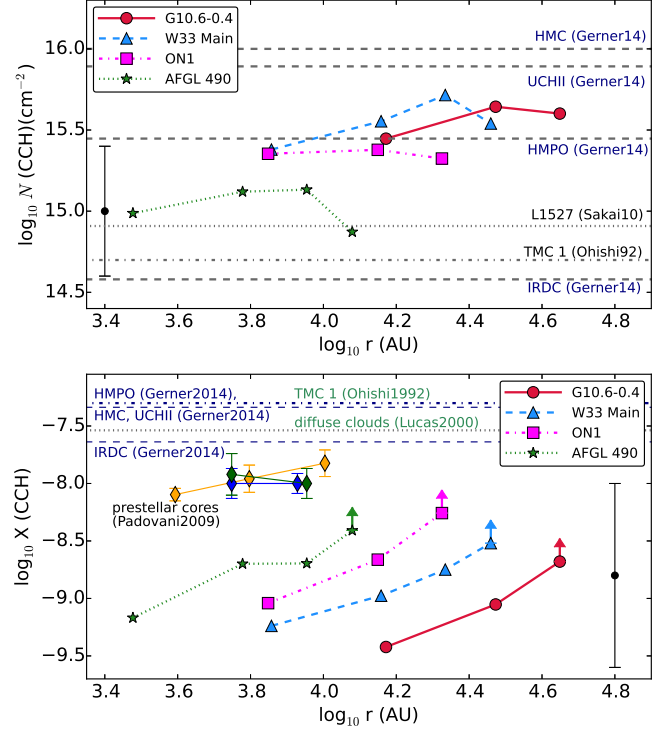


Figure 5. *Top:* C₂H column density radial profiles in logarithm scale of the four sources. Horizontal axis is the distance from the continuum peaks in units of AU. The typical error on the $N(\text{C}_2\text{H})$ is about 0.4 dex. The horizontal lines represent the $N(\text{C}_2\text{H})$ of other types of star forming regions (Germer et al. 2014; Sakai et al. 2010b). *Bottom:* C₂H abundance profiles. The points with arrows represent lower limits of the C₂H abundances. The error bar in the bottom right corner denotes the typical error on the C₂H abundances. On the top of the figure, the horizontal dashed lines represent the C₂H abundances from other works (Germer et al. 2014; Lee et al. 1998; Lucas & Liszt 2000). The diamonds on the upper left are the C₂H abundance profiles of the prestellar cores (Padovani et al. 2009). Colorful figures are available in the online version.

not affected significantly.

Figure 5 shows the $N(\text{C}_2\text{H})$ and $X(\text{C}_2\text{H})$ as a function of the separation (physical scale) from the 1.1 mm continuum peaks. For comparison, we also plot some $N(\text{C}_2\text{H})$ and $X(\text{C}_2\text{H})$ from other works in Figure 5. On the top panel, the horizontal reference lines denote the median $N(\text{C}_2\text{H})$ of different types of star formation regions obtained by Germer et al. (2014, dashed), the $N(\text{C}_2\text{H})$ of a low-mass star-forming region L1527 (dotted, Sakai et al. 2010b), and TMC 1 (dot dashed, Ohishi et al. 1992). Three of our sources have similar C₂H column densities as the HMPO, but slightly lower than the $N(\text{C}_2\text{H})$ of the UCHII in Germer et al. (2014). Note that the reference lines trace very different spatial scales as they represent single-dish observations. The $N(\text{C}_2\text{H})$ of AFGL 490 is lower than other sources, which might be due to the fact that the source is at a latter evolutionary stage when many molecules are destroyed by the ionizing radiation. For G10.6-0.4 and W33 Main the $N(\text{C}_2\text{H})$ in the centers are about a factor of two lower than their peak values, and overall the decreasing trend of $N(\text{C}_2\text{H})$ in the core centers of our targets is not very obvious.

The bottom panel of Figure 5 shows the $X(\text{C}_2\text{H})$ as a function of radius. We found that the $X(\text{C}_2\text{H})$ at

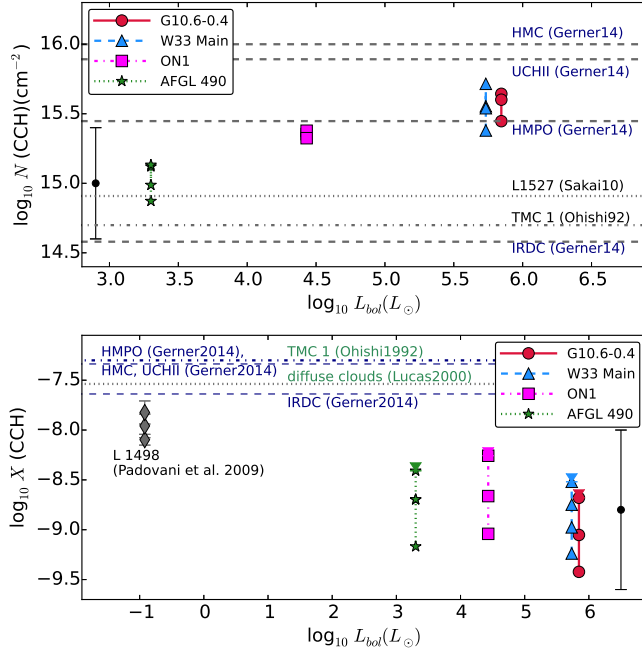


Figure 6. *Top:* C_2H column density, $N(\text{C}_2\text{H})$, as a function of bolometric luminosity. The symbols and reference lines are the same as in Figure 5. The typical error on the $N(\text{C}_2\text{H})$ is about 0.4 dex. *Bottom:* C_2H abundance $X(\text{C}_2\text{H})$ as a function of bolometric luminosity. The diamonds on the upper left are the C_2H abundance of the prestellar cores L1498 (Padovani et al. 2009), and its L_{bol} is from Shirley et al. (2005). Colorful figures are available in the online version.

larger separation are close to the values in the prestellar cores ($\sim 10^{-8}$, denoted as diamonds; Padovani et al. 2009) but lower than those of other types of clouds (reference lines). $X(\text{C}_2\text{H})$ systematically decreases toward the 1.1 mm continuum peaks by about one order of magnitude, and the four sources have similar slopes of the C_2H abundance radial profiles. Comparing the plots of $N(\text{C}_2\text{H})$ and $X(\text{C}_2\text{H})$ together we find that our derived $X(\text{C}_2\text{H})$ are lower than that of other work, and the inconsistency between our data and other work is mainly for the abundance plot.

Figure 6 plots $N(\text{C}_2\text{H})$ and $X(\text{C}_2\text{H})$ as a function of bolometric luminosities of the four sources. The top panel shows a trend that $N(\text{C}_2\text{H})$ increases in more luminous targets, and the more luminous sources G10.6-0.4 and W33 Main have the largest $N(\text{C}_2\text{H})$, despite the small sample and the uncertainty on $N(\text{C}_2\text{H})$. While the luminosities of the sources differ by nearly three orders of magnitude, their mean $N(\text{C}_2\text{H})$ differ only by about a factor of four. (see Section 4 for more discussion). On the other hand, the bottom panel of Figure 6 shows that $X(\text{C}_2\text{H})$ of our sample seem to be lower than the less luminous source L1498, which is a prestellar core. We again note that the uncertainty of $X(\text{C}_2\text{H})$ is large, although there is a plausible trend in the bottom panel of Figure 5 and 6.

4. DISCUSSION AND CONCLUSIONS

We used the SMA to observe the $\text{C}_2\text{H } N=3-2$ emission lines (~ 262 GHz) toward four high-mass star-forming regions G10.6-0.4, W33 Main, ON1 and AFGL 490 with a spatial resolution better than 0.15 pc scale. Our achieved

resolution is comparably smaller than the typical projected diameters of the HMCs, which is the key to examining the C_2H chemical evolution under the (proto)stellar illumination. Our results show that the extended C_2H emission traces the dense gas envelopes in these high-mass sources, and its column density $N(\text{C}_2\text{H})$ is of a few 10^{15}cm^{-2} .

Our observations show that, on ~ 0.15 pc scales, the C_2H emission peaks are systematically offset from the high-mass star-forming hot cores. This is consistent with the previous SMA observation of the source IRAS 18089-1732 (Beuther et al. 2008), as well as their model, which interprets such a scenario as the transformation of C_2H into other molecules in the dense and hot environment of the core center. The profiles in Figure 4 support such a proposed picture. Our findings of high column density C_2H are also in agreement with the single-dish survey by Gerner et al. (2014), in more luminous sources (Figure 6). This might be a natural result that more luminous sources have higher gas masses and a stronger PDR (photo-dominated region) effect. The age of the specific HMPO model presented in Beuther et al. (2008) was 5×10^4 yr, but since the ages of our observed sources are uncertain, and the abundance of C_2H cannot be derived very accurately at this moment, a direct comparison between the models and the observations remains difficult.

In Figures 5 and 6 we compare our derived $N(\text{C}_2\text{H})$ with that from the previous observations toward a sample of high-mass star-forming regions at different evolutionary stages (HMPO, HMC, and UCHII, Gerner et al. 2014). All sources Except for AFGL 490 show similar $N(\text{C}_2\text{H})$, which are close to the median $N(\text{C}_2\text{H})$ of the HMPO, but slightly lower than that of the UCHII. We note that in the work by Gerner et al. (2014) the C_2H data of the HMCs and UCHII (which are treated as later stages) were not well explained by the model, which might imply a more complicated chemistry of C_2H . $X(\text{C}_2\text{H})$ of the four sources are also compared with that of other clouds, including that from Gerner et al. (2014), the dark clouds TMC-1 and L134N, the prestellar cores, and the diffuse molecular clouds (Section 3.3). The abundances derived for our targets are significantly lower than those from other clouds, which is likely induced by the uncertainty of the interferometric observation. But note that the $X(\text{C}_2\text{H})$ of the prestellar cores (Padovani et al. 2009) are also lower than in those works, and their resolutions are comparable to the SMA (~ 0.15 pc) as their targets are much closer, so we suspect that the low $X(\text{C}_2\text{H})$ we find could also be a result of the difference between the physical resolution of the works.

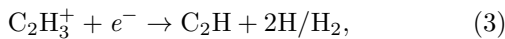
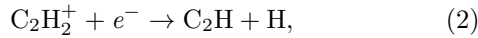
Figure 6 shows an increasing trend of $N(\text{C}_2\text{H})$ in more luminous sources, while in AFGL 490 the mean $N(\text{C}_2\text{H})$ is the lowest. Although AFGL 490 is still embedded in a molecular envelop, it is already in a transition stage to Herbig Be stars (Schreyer et al. 2006), so it is likely that the neutral molecular gas content of AFGL 490 has been reduced as a result of the ionized radiation. In fact, the reason for this trend in Figure 6 is likely that more luminous sources tend to have more molecular gas, but as our images (Figure 1) show, while C_2H is weaker in the central regions where it is possibly transformed, this trend show that the overall C_2H mass can maintain a certain

amount in the gas envelop surrounding the cores. This is also consistent with the picture that C₂H is a good tracer of PDR, in the sense that it traces the cloud surface illuminated by the stellar radiation (Meier & Turner 2005). It is also possible to compare this trend with that of other molecular lines to analyze the corresponding chemical process or radiation effect on molecules. Owing to the uncertainties mentioned above that cannot be accurately accounted for at this moment, the quantitative analysis of $X(\text{C}_2\text{H})$ is less conclusive, and it is unclear yet whether the abundance of C₂H is significantly affected by the bolometric luminosity. Short-spacing data are needed to improve the accuracy of the abundance, and higher-resolution observations can help to discern the genuine spatial structure of C₂H in different environments, as well as to provide additional information on the $\lesssim 10^4$ AU scales where models of different parameters start to deviate (Beuther et al. 2008).

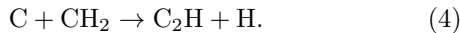
4.1. Chemistry of hydrocarbons

Observations toward the PDR region MonR2 found that C₂H is extended compared to CH and c-C₃H₂, and the abundance of C₂H is constant over a wide range of G_0 (UV intensity; Pilleri et al. 2013). They demonstrated that the behavior of C₂H is dominated by time-dependent effects and gas-grain chemistry in low-density molecular envelopes. This scenario agrees with our observations, which also show evidence that C₂H is stronger in the molecular envelopes.

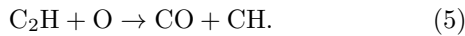
The formation of C₂H is mainly determined by the formation and evolution of ionized hydrocarbons, which involves the association of C⁺ and H₂: $\text{C}^+ \rightarrow \text{CH}_n^+$ ($n = 2, 3, 4, 5$). CH_{*n*}⁺ can be transformed into CH₄, then C₂H₂⁺ and C₂H₃⁺. C₂H is formed from the dissociated recombination of C₂H₂⁺ and C₂H₃⁺ (see, e.g., Turner et al. 2000; Meier & Turner 2005; Beuther et al. 2008, for details):



Other pathways of producing C₂H include the photodissociation of acetylene (C₂H₂), and the reaction between CH₂ and carbon atoms (Sakai et al. 2010b):



On the other hand, C₂H is mainly destroyed by the reactions with oxygen atoms:



It can also be transformed into a heavier carbon chain such as C₅ (Mookerjee et al. 2012). Models addressing the variation of gas-phase [C]/[O] abundance ratio (e.g., Terzieva & Herbst 1998) might help constrain the process of production/depletion of C₂H in these sources.

It would be also interesting to compare C₂H with other simple carbon chain molecules such as HC₃N, since they share the same chemical precursor C₂H₂⁺ (Wootten et al. 1980). Our observation covered HC₃N $J = 30 - 29$ simultaneously but its high excitation energy ($E_u \sim 200$ K) makes it difficult to compare its chemistry with C₂H $N = 3 - 2$ ($E_u \sim 25$ K) because they trace the distinct physical conditions. Observations at 3 mm band

would be able to cover both C₂H 1-0 (87.4 GHz) and HC₃N 10-9 (91 GHz, $E_u \sim 24$ K) simultaneously, and such comparison is more suitable for studying the chemistry of carbon chain molecules in cold gas. The comparison between C₂H and other molecular lines and related chemistry will be further addressed in future work.

4.2. Extragalactic perspective

Our derived $N(\text{C}_2\text{H})$ can also be compared with studies on external galaxies. Observation of 1 kpc scale molecular complex in M51 by Watanabe et al. (2014) found that $N(\text{C}_2\text{H})$ is a few times 10^{14} cm^{-2} (emission size corrected, corresponding $X(\text{C}_2\text{H})$ is about $\sim 4.5 - 5 \times 10^{-9}$), which is about an order of magnitude lower than the average $N(\text{C}_2\text{H})$ of the sources in our work. This might suggest that while C₂H has higher column density near PDRs on $\sim \text{pc}$ scales, and observations on large scales ($\sim 1 \text{ kpc}$) would mainly collect C₂H emission from those diffuse molecular gas.

In the high-resolution line surveys by Meier & Turner (2005, 2012); Meier et al. (2015), C₂H appears to be bright (comparable to CS in NGC 253) and well traces the circumnuclear PDR regions of the nearby galaxies, and even traces the molecular outflow in the nucleus of Maffei 2 (Meier & Turner 2012). The hyperfine structures of C₂H can help estimate the optical depth, and the frequency of C₂H 1-0 is very close to HCN 1-0 and HCO⁺ 1-0, so they can be observed simultaneously, and their different critical densities and chemical properties can be compared to diagnose the environment of galaxies. Jiang et al. (2011) have reported a sample of active galaxies detected in C₂H with the IRAM 30m telescope, and with the aid of ALMA and other facilities, the role of C₂H in studying extragalactic molecular gas will be further explored.

We acknowledge the SMA staff for their help during and after the observations. X.J. thanks Keping Qiu for informative discussions on the source ON1. This work is supported under the National Natural Science Foundation of China (grants 11390373, 11273015, 11133001, and 11328301), the Strategic Priority Research Program “The Emergence of Cosmological Structures” of the Chinese Academy of Sciences (grant XDB09000000), the National Basic Research Program (973 program No. 2013CB834905), and Specialized Research Fund for the Doctoral Program of Higher Education (20100091110009). Z.-Y.Z. acknowledges support from the European Research Council (ERC) in the form of Advanced Grant COSMICISM. This research made use of Matplotlib (Hunter 2007) and APLpy, an open-source plotting package for Python hosted at <http://aplpy.github.com>.

REFERENCES

- Beuther, H., Churchwell, E. B., McKee, C. F., & Tan, J. C. 2007, *Protostars and Planets V*, 165
- Beuther, H., Schilke, P., Menten, K. M., et al. 2002, *ApJ*, 566, 945
- . 2005, *ApJ*, 633, 535
- Beuther, H., Semenov, D., Henning, T., & Linz, H. 2008, *ApJ*, 675, L33
- Chapman, J. F., Millar, T. J., Wardle, M., Burton, M. G., & Walsh, A. J. 2009, *MNRAS*, 394, 221

- De Beck, E., Lombaert, R., Agúndez, M., et al. 2012, *A&A*, 539, A108
- Dyck, H. M., & Simon, T. 1977, *ApJ*, 211, 421
- Galván-Madrid, R., Keto, E., Zhang, Q., et al. 2009, *ApJ*, 706, 1036
- Galván-Madrid, R., Liu, H. B., Zhang, Z.-Y., et al. 2013, *ApJ*, 779, 121
- Gerin, M., Kaźmierczak, M., Jastrzebska, M., et al. 2011, *A&A*, 525, A116
- Gerner, T., Beuther, H., Semenov, D., et al. 2014, *A&A*, 563, A97
- Guélin, M., Neining, N., Lucas, R., & Cernicharo, J. 1999, in *The Physics and Chemistry of the Interstellar Medium*, ed. V. Ossenkopf, J. Stutzki, & G. Winnewisser, 326
- Haschick, A. D., & Ho, P. T. P. 1983, *ApJ*, 267, 638
- Herbst, E., & van Dishoeck, E. F. 2009, *ARA&A*, 47, 427
- Ho, P. T. P., & Haschick, A. D. 1981, *ApJ*, 248, 622
- . 1986, *ApJ*, 304, 501
- Hunter, J. D. 2007, *Computing In Science & Engineering*, 9, 90
- Hunter, T., & Brogan, C. 2006, <https://safe.nrao.edu/wiki/bin/view/Main/>
- Imanishi, M., & Nakanishi, K. 2014, *AJ*, 148, 9
- Immer, K., Galván-Madrid, R., König, C., Liu, H. B., & Menten, K. M. 2014, *ArXiv e-prints*, arXiv:1409.7125
- Immer, K., Reid, M. J., Menten, K. M., Brunthaler, A., & Dame, T. M. 2013, *A&A*, 553, A117
- Jiang, X., Wang, J., & Gu, Q. 2011, *MNRAS*, 418, 1753
- Keto, E. R., Ho, P. T. P., & Haschick, A. D. 1987, *ApJ*, 318, 712
- . 1988, *ApJ*, 324, 920
- Krumholz, M. R., Bate, M. R., Arce, H. G., et al. 2014, *ArXiv e-prints*, arXiv:1401.2473
- Kumar, M. S. N., Davis, C. J., & Bachiller, R. 2003, *Ap&SS*, 287, 191
- Kumar, M. S. N., Tafalla, M., & Bachiller, R. 2004, *A&A*, 426, 195
- Lahuis, F., & van Dishoeck, E. F. 2000, *A&A*, 355, 699
- Lee, H. H., Roueff, E., Pineau des Forets, G., et al. 1998, *A&A*, 334, 1047
- Li, J., Wang, J., Gu, Q., Zhang, Z.-Y., & Zheng, X. 2012, *ApJ*, 745, 47
- Liszt, H. S. 1995, *ApJ*, 442, 163
- Liu, H. B., Ho, P. T. P., & Zhang, Q. 2010, *ApJ*, 725, 2190
- Liu, H. B., Ho, P. T. P., Zhang, Q., et al. 2010, *ApJ*, 722, 262
- Liu, H. B., Jiménez-Serra, I., Ho, P. T. P., et al. 2012a, *ApJ*, 756, 10
- Liu, H. B., Quintana-Lacaci, G., Wang, K., et al. 2012b, *ApJ*, 745, 61
- Liu, H. B., Zhang, Q., & Ho, P. T. P. 2011, *ApJ*, 729, 100
- Liu, T., Wu, Y., Wu, J., Qin, S.-L., & Zhang, H. 2013, *MNRAS*, 436, 1335
- Lu, X., Zhang, Q., Liu, H. B., Wang, J., & Gu, Q. 2014, *ApJ*, 790, 84
- Lucas, R., & Liszt, H. S. 2000, *A&A*, 358, 1069
- MacLeod, G. C., Scalise, Jr., E., Saedt, S., Galt, J. A., & Gaylard, M. J. 1998, *AJ*, 116, 1897
- McMullin, J. P., Waters, B., Schiebel, D., Young, W., & Golap, K. 2007, in *Astronomical Society of the Pacific Conference Series*, Vol. 376, *Astronomical Data Analysis Software and Systems XVI*, ed. R. A. Shaw, F. Hill, & D. J. Bell, 127
- Meier, D. S., & Turner, J. L. 2005, *ApJ*, 618, 259
- . 2012, *ApJ*, 755, 104
- Meier, D. S., Walter, F., Bolatto, A. D., et al. 2015, *ApJ*, 801, 63
- Mitchell, G. F., Lee, S. W., Maillard, J.-P., et al. 1995, *ApJ*, 438, 794
- Mookerjee, B., Hassel, G. E., Gerin, M., et al. 2012, *A&A*, 546, A75
- Mueller, K. E., Shirley, Y. L., Evans, II, N. J., & Jacobson, H. R. 2002, *ApJS*, 143, 469
- Müller, H. S. P., Schlöder, F., Stutzki, J., & Winnewisser, G. 2005, *Journal of Molecular Structure*, 742, 215
- Ohishi, M., Irvine, W. M., & Kaifu, N. 1992, in *IAU Symposium*, Vol. 150, *Astrochemistry of Cosmic Phenomena*, ed. P. D. Singh, 171
- Padovani, M., Walmsley, C. M., Tafalla, M., Galli, D., & Müller, H. S. P. 2009, *A&A*, 505, 1199
- Palau, A., Estalella, R., Girart, J. M., et al. 2007, *A&A*, 465, 219
- Pilleri, P., Treviño-Morales, S., Fuente, A., et al. 2013, *A&A*, 554, A87
- Sakai, N., Sakai, T., Hirota, T., & Yamamoto, S. 2010a, *ApJ*, 722, 1633
- Sakai, N., Saruwatari, O., Sakai, T., Takano, S., & Yamamoto, S. 2010b, *A&A*, 512, A31
- Sanna, A., Reid, M. J., Menten, K. M., et al. 2013, *arXiv:1312.3181*
- Schreyer, K., Henning, T., van der Tak, F. F. S., Boonman, A. M. S., & van Dishoeck, E. F. 2002, *A&A*, 394, 561
- Schreyer, K., Semenov, D., Henning, T., & Forbrich, J. 2006, *ApJ*, 637, L129
- Shirley, Y. L., Nordhaus, M. K., Grcevich, J. M., et al. 2005, *ApJ*, 632, 982
- Simon, M., Felli, M., Cassar, L., Fischer, J., & Massi, M. 1983, *ApJ*, 266, 623
- Sollins, P. K., Zhang, Q., Keto, E., & Ho, P. T. P. 2005, *ApJ*, 624, L49
- Su, Y.-N., Liu, S.-Y., & Lim, J. 2009, *ApJ*, 698, 1981
- Tan, J. C., Beltran, M. T., Caselli, P., et al. 2014, *ArXiv e-prints*, arXiv:1402.0919
- Terzieva, R., & Herbst, E. 1998, *ApJ*, 501, 207
- Tielens, A. G. G. M. 2013, *Reviews of Modern Physics*, 85, 1021
- Tucker, K. D., Kutner, M. L., & Thaddeus, P. 1974, *ApJ*, 193, L115
- Turner, B. E., Herbst, E., & Terzieva, R. 2000, *ApJS*, 126, 427
- Wang, K., Zhang, Q., Wu, Y., Li, H.-b., & Zhang, H. 2012, *ApJ*, 745, L30
- Wang, K., Zhang, Q., Testi, L., et al. 2014, *ArXiv e-prints*, arXiv:1401.4157
- Watanabe, Y., Sakai, N., Sorai, K., & Yamamoto, S. 2014, *ArXiv e-prints*, arXiv:1404.1202
- Watt, G. D., White, G. J., Millar, T. J., & van Ardenne, A. 1988, *A&A*, 195, 257
- Wilson, S., & Green, S. 1977, *ApJ*, 212, L87
- Wootten, A., Bozayan, E. P., Garrett, D. B., Loren, R. B., & Snell, R. L. 1980, *ApJ*, 239, 844
- Xu, Y., Li, J. J., Reid, M. J., et al. 2013, *ApJ*, 769, 15
- Zhang, Q., Wang, Y., Pillai, T., & Rathborne, J. 2009, *ApJ*, 696, 268
- Zinnecker, H., & Yorke, H. W. 2007, *ARA&A*, 45, 481